

Diffraction of 0.5 keV electrons from free-standing transmission gratings

Ben McMorran^{a,*}, John D. Perreault^a, T.A. Savas^b, Alex Cronin^a

^a*Department of Physics, University of Arizona, 1118 E. 4th St, Tucson, AZ 85721, USA*

^b*Department of Engineering, Massachusetts Institute of Technology, 77 Massachusetts Ave., Cambridge, MA 92139, USA*

Received 11 January 2005; received in revised form 31 October 2005; accepted 11 November 2005

Abstract

A nanostructured grating was used to diffract a low-energy (500 eV) electron beam, and the current transmitted into the zeroth diffraction order was greater than 5% of the incident beam current. This diffraction efficiency indicates that the 55-nm-wide grating bars absorb electrons but the 45-nm-wide slots between bars transmit electron de Broglie waves coherently. The diffraction patterns can be asymmetric, and can be explained by a model that incorporates an electrostatic potential energy for electrons within 20 nm of the grating structure calculated by the method of images.

© 2005 Elsevier B.V. All rights reserved.

PACS: 61.14

Keywords: Low voltage electron diffraction; Electron holography; Electron interferometry; Inelastic scattering; Image-charge; Nanostructures; Nanofabrication

1. Introduction

We report on the diffraction of 500 eV electrons using 100-nm period fabricated transmission gratings with free-standing bars. The bars are separated by complete perforations that allow electrons to be efficiently transmitted and diffracted by these structures. The observed diffraction patterns are significant because they indicate that fabricated gratings could be useful beam splitters for electron interferometry. Our goal in this paper is to explain the main features of the diffraction patterns by using a model based on image-charge interactions.

To analyze the grating transmission function, the diffraction results are compared to a model that treats the grating bars as an absorption mask and the slots between the grating bars as a phase mask. The description of the bars as an absorbing mask is justified by simulations of electron trajectories inside the grating bar material. The

description of the slots as a phase mask is justified by the WKB approximation for electron de Broglie wave phase shifts and a model for potential energy due to image-charges in the slot walls. This model is similar to recent work on atom diffraction with nano-structure gratings [1,2], but the atom-surface (van der Waals) interaction in this case is replaced by an electron-surface (image-charge) interaction. We test this model by comparison to measured diffraction patterns obtained at different energies and with different angles of incidence. Measurements of the current in the zeroth order compared to the incident beam current, I_0/I_{inc} , are also used to test this model. It is noteworthy that the model for electron wave phase shifts presented here explains the asymmetric diffraction patterns observed when the gratings are used at non-normal angles of incidence as shown in Fig. 1.

The need for a high quality beam splitter for electron holography and interferometry motivates this work. While electrostatic biprisms [3] provide an elegant means of electron wavefront division, an electron beam with much less coherence can be used for interferometry if a

*Corresponding author. Tel.: +1 520 621 2688; fax: +1 520 621 4721.
E-mail address: mcmorran@physics.arizona.edu (B. McMorran).

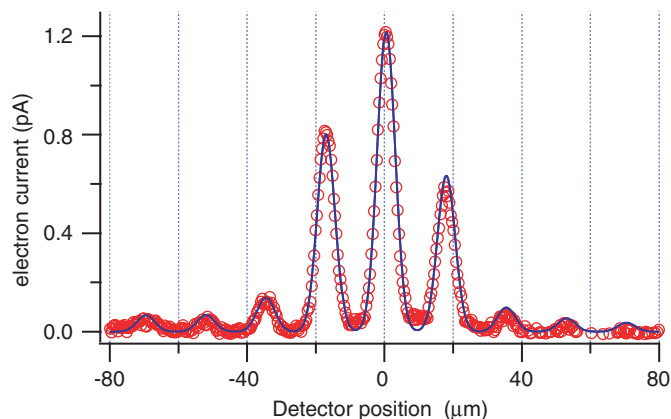


Fig. 1. A 500 eV electron diffraction pattern from a 100-nm period grating. The incident beam current was 25 pA and the angle of incidence was 1.5° . The data (dots) are compared to a model (solid line) for diffraction that includes the image-charge interaction with grating bars described by Eq. (12).

diffraction grating is used as an amplitude-dividing beam splitter [4]. To demonstrate this, Mertens et al. built an interferometer using a gold crystal as an electron beam splitter [5]. However, according to Mertens et al. “The main factor presently hampering the formation of high contrast hologram fringes is the quality of the beam splitter” [5]. In addition, Mertens et al. predicted, “the availability of a large variety of production technologies for small silicon devices suggests that production of a high quality silicon beam splitter should be possible.” This paper is devoted to characterizing a nano-structure grating that may serve as a beam splitter.

It is also noteworthy that the gratings described here can diffract much lower energy electrons than the solid diffraction gratings studied in [5–8]. Gratings that are supported by a solid substrate, or gratings made from slabs of solid crystals, must be extremely thin in order to diffract low-energy electrons. If the solid material is thicker than a few nanometers then low-energy electrons undergo inelastic scattering, and this diminishes the probability of diffraction [9]. In particular, the inelastic mean free path decreases with decreasing electron energy in most solids so that at 0.5 keV the mean free path is typically only 1 nm [10]. Thicker slabs of solid material only work as efficient diffraction gratings for electrons that have a higher energy. For example, Mertens et al. used a 60-nm-thick gold crystal as a beam splitter for 300 keV electrons [5], Ito et al. used fabricated arrays of holes of varying depths etched in 70-nm-thick AlF_3 films to diffract 200 keV electrons [6,7], and Drummy et al. reported diffraction of 4.7 keV electrons from 40 nm slabs of polyethylene crystals [8]. However, transmission diffraction gratings are not readily available for electrons with energy as low as 0.5 keV as reported here.

To distinguish this work from established techniques of Low Energy Electron Diffraction (LEED) and Electron Back Scatter Diffraction (EBSD), let it be emphasized that LEED and EBSD work in reflection mode. The reflection

geometry in LEED and EBSD setups is not amenable to transmission holography arrangements used by Mertens [5] or proposed by Missiroli [11] and Pozzi [12,13]. Also, while similar gratings have been used for Low Energy Electron Beam Proximity Projection Lithography (LEEPL) [14], LEEPL takes place in the extreme near-field with the goal of minimizing diffraction effects.

2. Free-standing gratings

The grating structures shown in Figs. 2 and 3 are made from silicon nitride by Savas and Smith at the MIT NanoStructures laboratory using achromatic interferometric lithography. The fabrication procedure is described in Refs. [15,16]. Standing waves of light with a 100-nm period (from an ArF laser, $\lambda = 193$ nm) were used to expose a photo-resist coating on top of a 120-nm-thick membrane of silicon nitride. Reactive ion etches were then used to form free-standing 55-nm-wide bars of silicon nitride by etching slots completely through the membrane. The bars span $1.1 \mu\text{m}$ between perpendicular ‘support bars’ that are repeated every $1.5 \mu\text{m}$ as shown in Fig. 2. This free-standing mesh structure extends over an area of

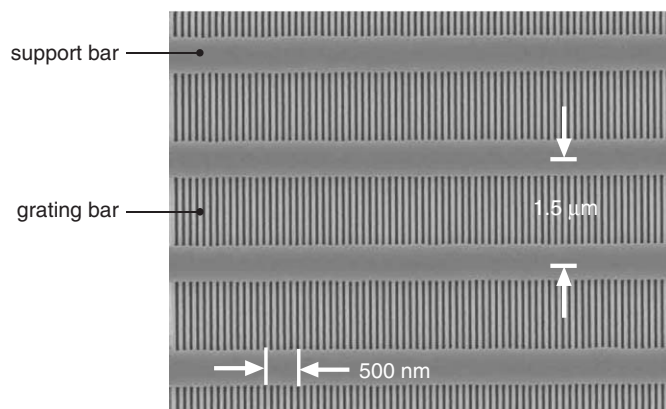


Fig. 2. Front view of a 100-nm period grating. The dark regions are slots and the light areas are free-standing bars. To observe diffraction the probe beam is focused 3 cm beyond the grating plane.

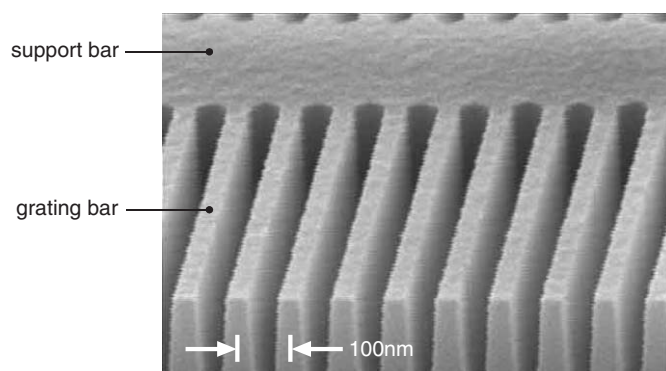


Fig. 3. Perspective view of a grating that was cleaved. Note the trapezoidal cross-section of the bars.

1 mm × 3 mm inside a frame, making approximately 10,000 free-standing grating bars across the grating. The bars are slightly trapezoidal in cross section as shown in Fig. 3.

Similar gratings are used for atom and molecule interferometry [17]. The grating bars were sputter-coated with approximately 2 nm of Au/Pd metal for use with an electron beam. Without the metal coating no electron diffraction was observed, and this can be explained by irregular charging of the grating bars. When the gratings are metal-coated, we can observe electron diffraction patterns as shown in Fig. 1.

3. Electron transmission simulations

Monte Carlo simulations using the Casino software [18] indicate that at energies below 3 keV, no electrons pass through a 120-nm-thick slab of silicon nitride (see Figs. 4 and 5). Scattered electrons and secondary electrons may be emitted from the front surface and edges of a grating bar, however only electrons that have undergone zero inelastic scattering events can interfere to form a diffraction pattern. The results displayed in Fig. 5 indicate that all electrons transmitted through the bars undergo at least one inelastic collision unless the incident beam energy

exceeds several tens of keV. Furthermore, we have shown experimentally that the inelastically scattered electrons can be distinguished from the diffraction pattern by using apertures (as shown in Fig. 8) because the trajectories of scattered electrons are distributed over 1 rad as compared to the diffraction angle of order 10^{-4} rad.

Even though the scattering simulations in Fig. 4 were conducted for beams at normal incidence to a solid slab of material, the simulations indicate that grating bars will function as an absorbing mask for coherent low-energy electrons regardless of the angle of incidence. This is because transmission of 500 eV electrons without scattering is only probable for paths that traverse less than 1 nm in the grating bar material.

4. Image-charge model

This nano-structure grating has open slots that are perforated entirely through the structure. So, when it is oriented near normal incidence, a fraction of the incident beam is transmitted through the slots and does not come in contact with solid material. Still, as electrons pass through the slots they can interact with the grating structure at a distance via electric fields. In this section we describe how

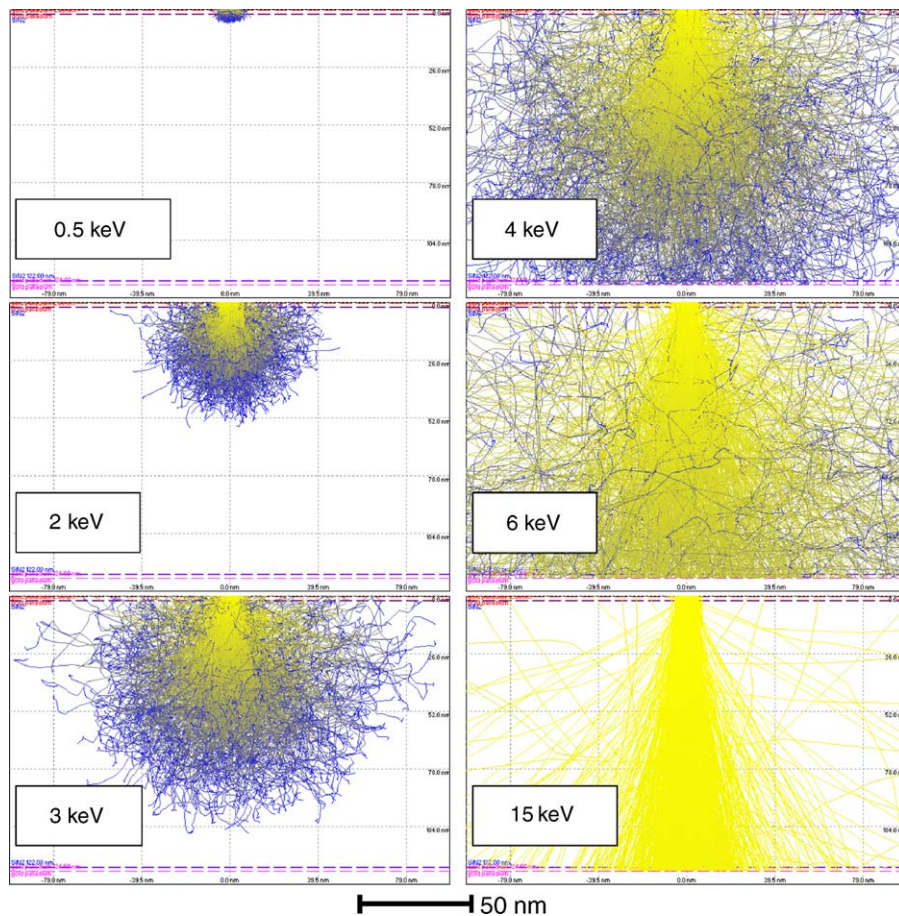


Fig. 4. Monte Carlo simulation of the paths taken by 1000 electrons normally-incident on a 120 nm silicon nitride membrane coated on both sides with 2 nm of Au/Pd. Simulations are shown for six different incident beam energies. The brightness of each path corresponds to the energy of the electron relative to the incident beam energy.

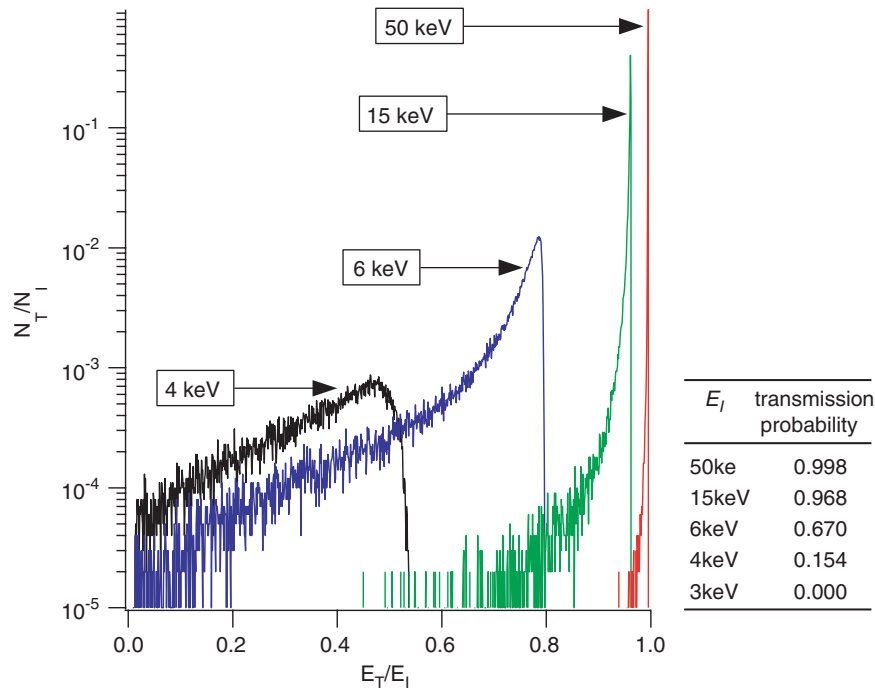


Fig. 5. (Left) Probability distribution of electrons transmitted through a 120-nm-thick slab of grating bar material, as a function of their exit energy E_T for four different incident beam energies E_I . (Right) The total transmission probability, integrated over all energies. For these Monte Carlo simulations 10^5 electron trajectories were used.

the electrostatic potential energy for the electrons in free space near a dielectric surface will perturb the electron de Broglie waves, and predict how phase shifts that depend on position within each slot will modify the diffraction patterns.

The potential energy for an electron in the free-space between grating bars is approximately given by the potential from two image-charges written in Gaussian units as

$$U = -e^2 \left(\frac{1}{2r_1} + \frac{1}{2r_2} \right) \left(\frac{\epsilon - 1}{\epsilon + 1} \right), \quad (1)$$

where r_1 and r_2 are the altitudes from the two inner surfaces as shown in Fig. 6, $-e$ is the charge of the electron, and ϵ is the ratio of the permittivity of the grating material to the permittivity of free space; the image-charge is $+e(\epsilon - 1)/(\epsilon + 1)$. For an ideal conductor $\epsilon = \infty$, the image-charge is $+e$, and the energy due to the image-charge 1 nm from a surface is $U = -0.75$ eV.

This model ignores multiple reflections of image-charges. This is justified because the set of all image-charges modifies the potential due to only the first reflection by at most 35% (when the charge is centered in the channel), but modifies the potential *gradient* by at most 0.5%. As it turns out, the gradient of the potential, i.e. the force due to the image-charges, is most significant for the diffraction results presented here. Although the method of images is for electrostatic problems, it is approximately valid for situations involving slow-moving electrons. This is discussed in Ref. [19]. We find that a full dynamical

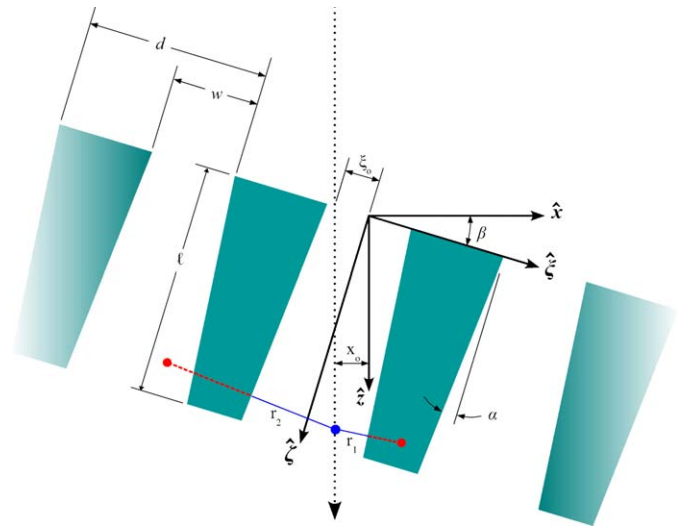


Fig. 6. Schematic view of a grating in cross section. The $\hat{\xi}$ -axis is normal to the grating and the \hat{x} -axis is parallel to the grating wavevector. An electron is shown along a path (dotted line) that is incident at an angle β and enters a grating slot with offset ξ_0 . The electron interacts with two image-charges as it passes between the free-standing bars. The \hat{x} - and \hat{z} -axes shown here are the same as in Fig. 8.

treatment of surface effects is not needed in order to reproduce the velocity-dependent asymmetry and diffraction efficiencies we observed.

We will use two coordinate systems. One has $\hat{\xi}$ normal to the grating and \hat{x} along the grating wavevector. The second coordinate system has \hat{z} parallel to the incident electron

beam velocity and \hat{x} perpendicular to it. The $\hat{\zeta}$ and $\hat{\xi}$ axes are tilted at the angle of incidence, β , with respect to the \hat{z} - and \hat{x} -axes as shown in Fig. 6.

In the Raman–Nath (also known as thin phase mask) and WKB approximations to leading order in U/E (where E is the kinetic energy) the phase shift due to the potential U is related to the integral of the potential along straight-line paths in the \hat{z} direction

$$\begin{aligned}\phi(\beta, \xi_0) &= \frac{-1}{v\hbar} \int_{-\infty}^{\infty} U dz \\ &\approx \frac{-1}{v\hbar \cos \beta} \int_0^{\ell} U(\beta, \xi_0, \zeta) d\zeta,\end{aligned}\quad (2)$$

where ξ_0 describes the position of a path at the entrance to a grating slot (where $\zeta = 0$), v is the velocity of the particle, ℓ is the grating thickness, and we have made the substitution $\zeta = z/\cos \beta$. Here the geometric parameters (β , ξ_0 , and the grating wedge angle α) are implicitly used to relate r_1 and r_2 in Eq. (1) to the depth of the electron within the grating slot, ζ , as shown in Fig. 6. This model assumes a potential due to two infinite planes while the electron is passing through the grating slots, and completely ignores edge effects at the entrance and exit, as indicated by the limits of integration in Eq. (2).

By symmetry the equations describing the potential due to each wall are identical, with parameters β and ξ_0 having opposite signs. We can separate the total phase shift into contributions from each wall

$$\phi(\beta, \xi_0) = \delta(\beta, \xi_0) + \delta(-\beta, -\xi_0), \quad (3)$$

where $\delta(\beta, \xi_0)$ is the phase shift due to an interaction with one inner surface and $\delta(-\beta, -\xi_0)$ is due to the other. Performing the integration in Eq. (2), the explicit form of $\delta(\beta, \xi_0)$ is

$$\begin{aligned}\delta(\beta, \xi_0) &= \frac{-e^2 \left(\frac{\varepsilon - 1}{\varepsilon + 1} \right)}{2v\hbar \sin(\alpha + \beta)} \\ &\times \ln \left[\frac{\frac{w}{2} + \xi_0 + \ell(\tan \alpha + \tan \beta)}{\frac{w}{2} + \xi_0} \right].\end{aligned}\quad (4)$$

This is the phase shift acquired by an electron wave propagating along a path described by $\xi(\zeta) = \xi_0 + \zeta \tan \beta$ due to a single grating wall of a slot that has a length of ℓ , a slot width w , and wedge angle α . The total phase shift, $\phi(\xi)$, is the sum of phase shifts due to both inside surfaces (Eq. (3)). This phase shift calculation is identical to the one outlined by Cronin and Perreault [1], with the exception that for atoms the phase is acquired because of a van der Waals potential that depends on $U \propto 1/r^3$, and here we are concerned with an image-charge potential that depends on $U \propto 1/r$ (which gives rise to the logarithm in Eq. (4)). A cartoon of phase fronts perturbed by a grating is shown in Fig. 7. We assume a plane wave is incident on the grating, and the phase fronts of the wave transmitted through the grating are described by $\phi(\beta, \xi_0)$ from Eqs. (3) and (4).

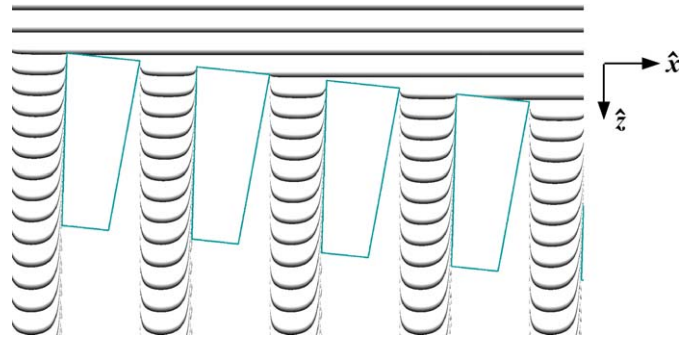


Fig. 7. Schematic representation of the wave front curvature caused by the image-charge effect. The additional phase of the propagating wave front is described by the function $\phi(\beta, \xi_0)$ in Eqs. (3) and (4).

To calculate the electron wavefunction $\psi(x, z)$ in the far field, where the diffraction pattern is observed (at $z = L \approx 3$ mm), we first determine the wavefunction immediately after the grating (where $z = \ell \approx 120$ nm) in the Raman–Nath and WKB approximations,

$$\psi(x, \ell) = \psi(x, 0) \left[T(\beta, x) * \text{comb} \left(\frac{x}{d \cos \beta} \right) \right]. \quad (5)$$

The electron wavefunction incident on the grating, $\psi(x, 0)$, is multiplied by the convolution of a complex transmission function $T(\beta, x)$ with an array of delta functions that are spaced by $d \cos \beta$. The comb function represents how the grating transmission function is periodic. The complex transmission function for a single grating period is

$$T(\beta, x) = \exp[i\phi(\beta, x)] \Theta(x - x_{\min}) \Theta(x_{\max} - x), \quad (6)$$

where the Heaviside functions Θ describe absorption by the bars on either side of a slot, and the complex term, $\exp[i\phi(\beta, x)]$, is due to the grating-induced phase shift given by Eqs. (3) and (4) and the change of variables $\xi_0 \cos(\beta) = x$. The arguments of the Heaviside functions describe the locations of the bar edges that serve as apertures for each slot, with x_{\min} and x_{\max} given by geometry (see Fig. 8).

$$x_{\min} = -\frac{w}{2} \cos \beta, \quad (7)$$

$$x_{\max} = \begin{cases} \frac{w}{2} \cos \beta, & \beta \leq \alpha, \\ \frac{w}{2} \cos \beta + \ell(\tan \alpha - \tan \beta), & \beta > \alpha. \end{cases} \quad (8)$$

The wavefunction in the far-field, $\psi(x', L)$, is given by a scaled Fourier transform (which is a Fourier optics technique described in Ref. [20])

$$\psi(x', L) = N \mathcal{F} \{ \psi(x, \ell) \}_{f_x = x'/\lambda L}, \quad (9)$$

where N is a normalization constant, the primed variable x' denotes the lateral position in the far-field, $\mathcal{F} \{ \}_{f_x}$ is a Fourier transform using f_x as the conjugate variable to x , and λ is the de Broglie wavelength. Noting that $\psi(x, \ell)$ is given by a product and a convolution (Eq. (5)), the far-field

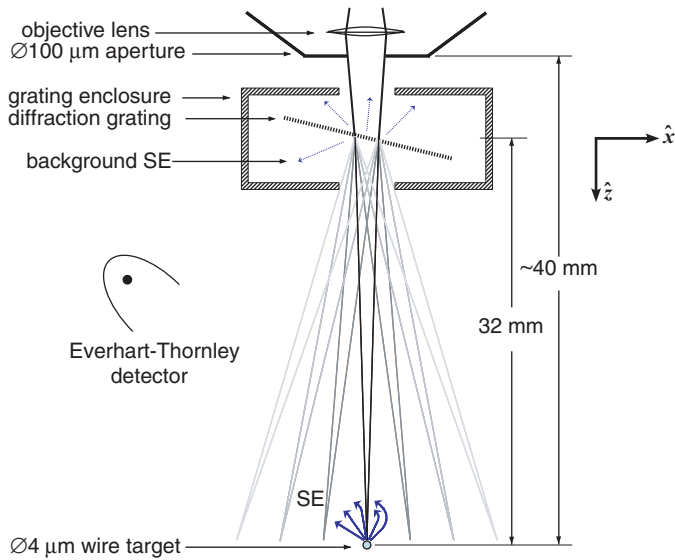


Fig. 8. Schematic of the objective lens, diffraction grating, and target wire. The secondary electron (SE) signal generated on the target wire was detected with an Everhart–Thornley detector. Secondary electrons generated at the grating produce a background signal that was minimized by surrounding the grating with a conductive enclosure.

wavefunction becomes

$$\psi(x', L) = N \mathcal{F}\{\psi(x, 0)\} * \left[\mathcal{F}\{T(\beta, x)\} \cdot \mathcal{F}\left\{\text{comb}\left(\frac{x}{d \cos \beta}\right)\right\} \right] \Big|_{f_x=x'/\lambda L}, \quad (10)$$

where we have used the convolution theorem. The diffraction pattern for the electron flux is then

$$I(x') = |\psi(x', L)|^2 = \sum_{j=-\infty}^{\infty} I_j S\left(x' - j \frac{\lambda L}{d \cos \beta}\right), \quad (11)$$

where I_j is the intensity of the j th diffraction order

$$I_j = I_{\text{inc}} \left| \int_{x_{\text{min}}}^{x_{\text{max}}} \exp\left[i\left(\frac{2\pi}{d \cos(\beta)}\right)jx + i\phi(\beta, x)\right] dx \right|^2 \quad (12)$$

and the function

$$S(x') = |N \mathcal{F}\{\psi(x, 0)\}|_{f_x=x'/\lambda L}^2 \quad (13)$$

describes the beam profile repeated for each diffraction order in the detection plane located at $z = L$. From the argument of $S()$ in Eq. (11) we see that the diffracted probe spots are displaced from the central ($j = 0$) spot, to first-order in the diffraction angle, by the distance

$$x' = L \frac{j\lambda}{d \cos \beta} = L \frac{j}{d \cos \beta} \sqrt{\frac{1.5 \text{ eV}}{E}} \text{ \AA}, \quad (14)$$

where the de Broglie wavelength is $\lambda = h/p \approx (E/150 \text{ eV})^{-1/2} \text{ \AA}$, and E is the kinetic energy of an electron. In our experiments, $L = 32 \text{ mm}$, $d = 10^{-7} \text{ m}$,

and for a 500 eV electron beam $\lambda = 0.55 \text{ \AA}$, so at normal incidence the first-order diffracted probe spots are separated by $x' = 18 \mu\text{m}$ from the $j = 0$ probe spot. This is confirmed with the data shown in Figs. 1 and 10.

In Fig. 1 the data are directly compared to the prediction from Eq. (11) using a Gaussian with a best fit width of $\sigma = 2.4 \mu\text{m}$ for the beam profile $S(x')$. In Fig. 10 the theoretical diffraction envelopes I_j are shown by plotting pairs of values (I_j, x_j) given by Eqs. (12) and (14) for continuous values of j , even though the diffraction orders only occur for integer values of j . The theoretical diffraction envelopes for different energies and different angles of incidence are shown with dashed lines on the same axes as the data.

5. Diffraction experiments

An Hitachi S-2460N scanning electron microscope (SEM) was used to observe diffraction from a grating located in the electron beam as shown in Fig. 8. A tungsten ‘target wire’ with a diameter of $4 \mu\text{m}$ and an Everhart–Thornley detector were used to detect the focused electron beam 40 mm below the objective lens. The grating was mounted on a tip-tilt stage, grounded, and inserted 8 mm below the objective lens so the electron beam illuminated about 800 grating bars. The transmitted beam then formed multiple probe spots near the target wire due to diffraction, with each spot focused to approximately $1 \mu\text{m}$ and displaced by $18 \mu\text{m}$ according to Eq. (14). When the incident beam was scanned using the SEM scan coils, the entire diffraction pattern was translated with respect to the target wire.

The SEM images report secondary electron (SE) signals that are generated when the diffracted beams hit the target wire. An enclosure around the grating and a Faraday cup below the target wire minimized background signal due to SE generated at surfaces other than that of the target wire. The SE signal as a function of probe position is extracted from the images by averaging the values of pixels in columns to plot a line profile for each image as shown in Fig. 9. For beams with energy higher than 500 eV the spots can be focused to smaller diameters, but the size of the target wire limits how well the diffraction patterns are resolved.

Fig. 10 shows data obtained at three different beam energies (E) and at four different incident angles (β). The ‘‘horns’’ on the higher-energy diffraction peaks are due to the edge effect (the interaction volume of the beam in the target wire intersects more surface at an edge, producing more SE signal). The asymmetry of the diffraction orders is consistent with the model based on the image–charge interaction as shown by the theoretical diffraction envelopes (dashed curves) in Fig. 10.

The data are more asymmetric at lower beam energies. This is also predicted by the image–charge model because lower-velocity electrons acquire larger phase shifts. Furthermore, the asymmetry is observed to reverse sign

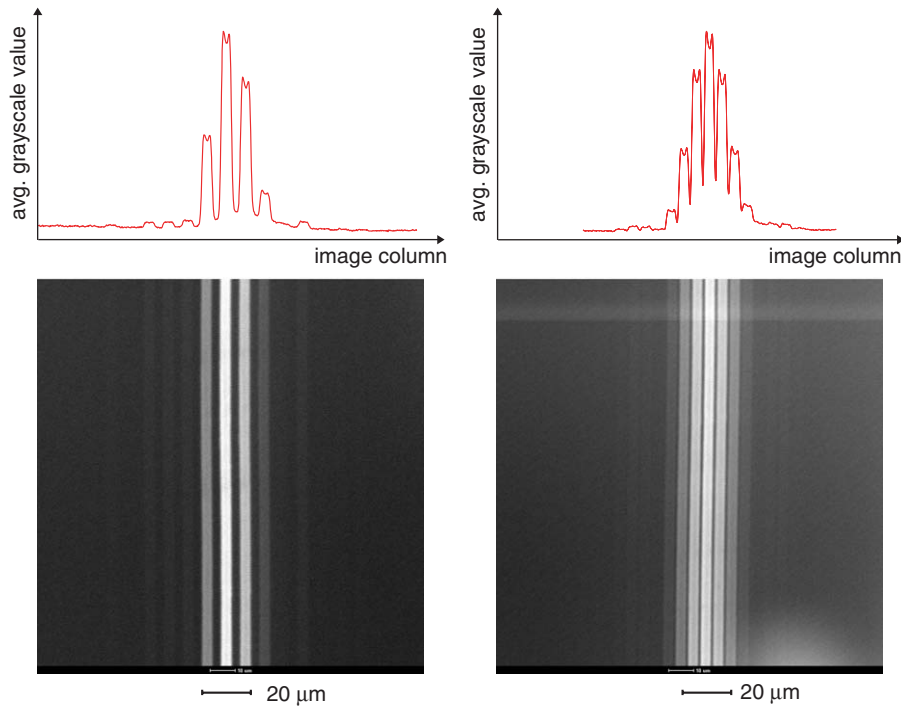


Fig. 9. Secondary electron (SE) images of a single wire obtained with a diffracted electron beam probe. (Left) The grating was tilted at approximately $5 \pm 3^\circ$, and a 1.5 keV accelerating voltage was used. (Right) The grating tilted at $10 \pm 2^\circ$ diffracted a 4 keV beam. Line profiles of secondary electron signal were generated from the images. The background was due to an object in the foreground and was subtracted by hand in the line profiles. Although the line profiles are proportional to the intensity in each order, their vertical axes are in arbitrary units that depend on SE production efficiency, detector contrast, image brightness, etc.

for angles of incidence with opposite sign. The image–charge model reproduces this too.

The best agreement with the data, determined by minimizing the sum of the squared errors (SSE) between measured and theoretical values of I_j , was obtained using the image–charge model with the image–charge set to $+(0.6 \pm 0.4)e$. The tilt angle (β) and wedge angle (α) were free parameters in the model, but fixed values of β were used for all the model results shown in each row of Fig. 10, and a single value of $\alpha = 4.5^\circ$ was used for all the curves presented here. The value of the image–charge $+(0.6 \pm 0.4)e$ corresponds to a most likely value of permittivity of 4, a lower bound on the permittivity of 1.7, and an upper bound of $\epsilon = \infty$.

To determine if the value for ϵ that minimizes the SSE is reasonable, it can be compared to the dielectric function at zero frequency for both gold and silicon nitride. The frequency dependent dielectric function for low-pressure chemical vapor deposited silicon nitride (grating bar material) is described in Refs. [2,21]. At zero frequency the dielectric function takes on a value of $\epsilon \approx 3.85$ which is in fair agreement with the value $\epsilon = 4$ obtained from the diffraction data. Since the gratings are coated with gold it is also worth noting that the dielectric function at zero frequency for bulk gold is $\epsilon \approx -1.13 \times 10^5$ [22]. This seems to suggest that although the gold coating prevents charging of the grating bars and enables the observation of the diffraction patterns, it does not significantly influence the

electron–surface interaction between the bars. A physical picture that could be consistent with this finding is that the front surface of the gratings are coated with a significant amount of gold, while the interior grating bar surfaces have very little gold coating.

To directly measure the current in each diffraction order, we replaced the target-wire with a Faraday cup behind an electrically grounded 6- μm -wide slit. By positioning the electron beam so that different parts of the diffraction pattern entered the Faraday cup, and repeating this measurement with the grating removed, we quantified the efficiency for diffraction into the zeroth order (I_0/I_{inc}) for several beam energies as shown in Fig. 11.

The theoretical diffraction efficiency (I_0/I_{inc}) for an absorbing grating at normal incidence ($\beta = 0$) with no image–charge potential [$\phi(0, x) = 0$] is a specific case of Eq. (12). The support structure acts as another absorption mask and further reduces the transmitted current. From these two considerations we expect $I_0 = I_{\text{inc}}(w/d)^2(w_s/d_s)$ where w and d are the grating slot width and grating period, respectively, w_s is the width of the space between support bars, and d_s is the spacing of the support bar structure. When the image–charge model is included, the diffraction efficiency is predicted to be

$$\frac{I_0}{I_{\text{inc}}} = \left(\frac{w}{d}\right)^2 \left(\frac{w_s}{d_s}\right) A(\epsilon, E, w, d, \beta, \alpha), \quad (15)$$

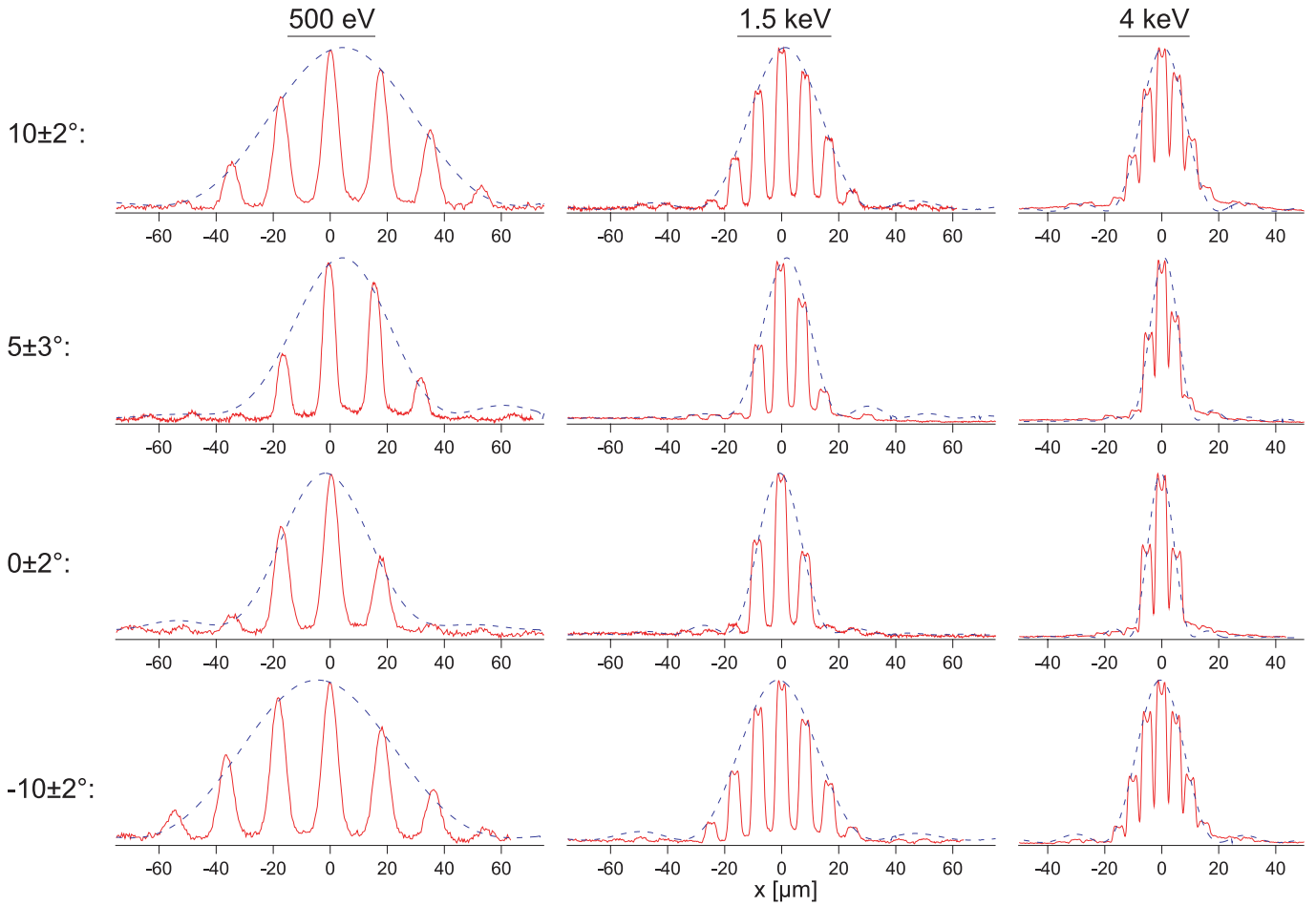


Fig. 10. Electron diffraction patterns (solid) with theoretical envelope functions (dotted). The beam energy (E) is constant within each column, and the incident angle (β) is constant within each row. Four additional parameters used in the theory for I_j (Eq. (12)) (namely $\varepsilon = 4$, $\ell = 120$ nm, $w = 44$ nm and $\alpha = 4.5^\circ$) were adjusted to minimize the difference between measured and theoretical values for I_j simultaneously for all the data shown.

where A is a function due to the image–charge interaction given from Eq. (12) to be

$$A(\varepsilon, E, w, d, \beta, \alpha) = \left| \int_{x_{\min}}^{x_{\max}} \exp[i\phi(\beta, x)] dx \right|^2. \quad (16)$$

The function A is nearly unity for energies above 10 keV and decreases significantly below unity for energies below 2 keV as shown in Fig. 11.

In our experiments, the grating bar window size is $w = 44$ nm and the period is $d = 100$ nm. The open space between support structure bars is $w_s = 1.1 \mu\text{m}$ and the support period is $d_s = 1.5 \mu\text{m}$, so the expected transmission efficiency into the zeroth order is 14.2% if $A = 1$. We find that the actual transmission efficiency into the zeroth order varies between 5% and 12% as a function of energy and this is reproduced by the image–charge model as shown in Fig. 11.

The background current (I_{bkg}) detected with the Faraday cup between the $j = 0$ and $j = 1$ diffraction orders was less than 0.1% of I_{inc} so the signal to background (I_0/I_{bkg}) is greater than 50.

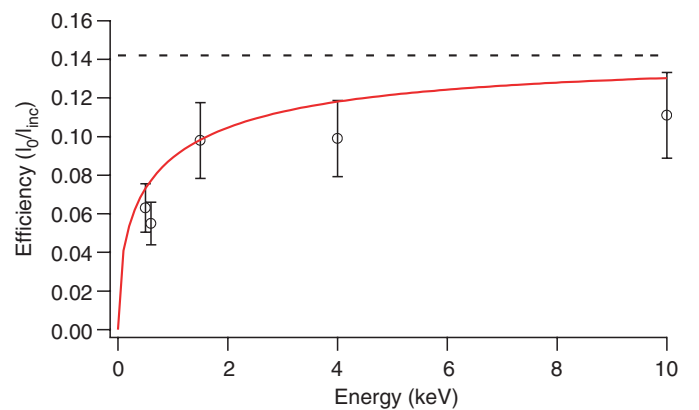


Fig. 11. Diffraction efficiency in the zeroth order (I_0/I_{inc}) measured at different energies (markers). The efficiency predicted with the image–charge model is shown (solid curve) for parameters ($w = 44$ nm, $\varepsilon = 4$, $\beta = 0$, $\alpha = 4.5^\circ$, $\ell = 120$ nm). The efficiency predicted without the image–charge (dashed line) uses the same parameters but $\varepsilon = 1$.

The incident beam current was $I_{\text{inc}} = 25$ pA (at $E = 500$ eV). At this beam energy the transit time through the grating ($\approx 10^{-15}$ s) is short compared to the rate at

which electrons enter the grating (10^8 s^{-1}), so only one electron at a time is transmitted through the grating. This emphasizes the fact that we are dealing with single electron diffraction and it is appropriate to neglect interactions between beam electrons. The maximum beam current we used (for imaging) was $I_{\text{inc}} = 2 \text{ nA}$ (at $E = 25 \text{ keV}$). Since this was raster scanned over regions as small as $(100 \text{ nm})^2$ this corresponds to a steady-state current density of $2 \times 10^5 \text{ A/m}^2$, and this did not appear to damage the grating.

6. Summary

In conclusion, we have demonstrated that nano-fabricated structures with free-standing bars can serve as a transmissive diffraction grating for low-energy (500 eV) electrons. We have analyzed the electron–grating interaction as a complex transmission function, and find that the nano-structure grating behaves both as an amplitude mask (due to inelastic scattering inside the grating bars), and also as a phase mask (due to electrostatic interactions with the grating surfaces). The asymmetry of the diffraction patterns ($I_j \neq I_{-j}$) and the efficiency of transmission diffraction into the zeroth order ($I_0/I_{\text{inc}} \geq 5\%$) are both consistent with the model based on this complex transmission function. This theoretical and experimental description of electron diffraction from nanostructures will help evaluate how nano-structure gratings can perform as beam splitters for electron interferometry.

Acknowledgements

We gratefully thank Gary Chandler for his support and instruction regarding our use of the SEM. This research

was supported by an Award from Research Corporation, NSF Grant ECS-0404350, and NSF Grant PHY-0354947.

References

- [1] A. Cronin, J. Perreault, *Phys. Rev. A* 70 (4) (2004) 043607.
- [2] J. Perreault, A. Cronin, T. Savas, *Phys. Rev. A* 71 (2005) 053612.
- [3] G. Mollenstedt, H. Duker, *Naturwissenschaften* 42 (1955) 41.
- [4] G. Matteucci, G. Missiroli, G. Pozzi, *Ultramicroscopy* 6 (1981) 109.
- [5] B. Mertens, M. Overwijk, P. Kruit, *Ultramicroscopy* 77 (1999) 1.
- [6] Y. Ito, A. Bleloch, L. Brown, *Nature* 394 (1998) 49.
- [7] Y. Ito, A. Bleloch, J. Patterson, L. Brown, *Ultramicroscopy* 52 (1993) 347.
- [8] L. Drummy, J. Yang, D. Martin, *Ultramicroscopy* 99 (2004) 247.
- [9] R. Al-Mausawe, T. Quinn, *J. Phys. D: Appl. Phys.* 15 (1982) 267.
- [10] D. Penn, *Phys. Rev. B* 35 (2) (1987) 482–486, see also: http://xdb.lbl.gov/Section3/Sec_3-2.html.
- [11] G. Missiroli, G. Pozzi, U. Valdrè, *J. Phys. E* 14 (1981) 649.
- [12] G. Pozzi, *Optik* 47 (1977) 105.
- [13] G. Pozzi, *Optik* 63 (1983) 227.
- [14] M. Yoshizawa, T. Savas, *Jpn. J. Appl. Phys. Part 2—Lett.* 41 (1A) (2002) L87.
- [15] T. Savas, S. Shah, M. Schattensburg, J. Carter, H. Smith, *J. Vac. Sci. Technol. B* 13 (6) (1995) 2732.
- [16] T. Savas, M. Schattensburg, J. Carter, H. Smith, *J. Vac. Sci. Technol. B* 14 (6) (1996) 4167.
- [17] P. Berman (Ed.), *Atom Interferometry*, Academic Press, San Diego, 1997.
- [18] A. Drouin, A. Couture, R. Gauvin, P. Hovington, P. Horny, H. Demers, *Casino* version 2.42, 2001, <http://www.gel.usherb.ca/casino/>
- [19] A. Rivacoba, N. Zabala, J. Aizpurua, *Prog. Surf. Sci.* 65 (2000) 1.
- [20] J. Goodman, *Introduction to Fourier Optics*, McGraw-Hill, New York, 1996.
- [21] R. Bruhl, P. Fouquet, R. Grisenti, J. Toennies, G. Hegerfeldt, T. Kohler, M. Stoll, C. Walter, *Europhys. Lett.* 59 (3) (2002) 357.
- [22] M. Ordal, L. Long, R. Bell, S. Bell, R. Bell, R. Alexander, C. Ward, *Appl. Opt.* 22 (7) (1983) 1099.